Enhancing Dry Adhesion of Polymeric Micropatterns by Electric Fields

Article *in* ACS Applied Materials & Interfaces · May 2020

DOI: 10.1021/acsami.0c05077

5 authors, including:

Vaishali Chopra
Universität des Saarlandes
2 PUBLICATIONS **39** CITATIONS
SEE PROFILE

René Hensel
INM - Leibniz Institute for New Materials
39 PUBLICATIONS **662** CITATIONS
SEE PROFILE

Anton A. Darhuber
Eindhoven University of Technology
139 PUBLICATIONS **2,966** CITATIONS
SEE PROFILE

Eduard Arzt
INM - Leibniz Institute for New Materials
472 PUBLICATIONS **18,951** CITATIONS
SEE PROFILE

ACS APPLIED MATERIALS & INTERFACES

www.acsami.org

Research Article

Enhancing Dry Adhesion of Polymeric Micropatterns by Electric Fields

Vaishali Chopra, Maciej Chudak, René Hensel, Anton A. Darhuber, and Eduard Arzt*

Cite This: *ACS Appl. Mater. Interfaces* 2020, 12, 27708–27716

Read Online

ACCESS | Metrics & More | Article Recommendations | Supporting Information

ABSTRACT: Micropatterned dry adhesives rely mainly on van der Waals interactions. In this paper, we explore the adhesion strength increase that can be achieved by superimposing an electrostatic field through interdigitated subsurface electrodes. Micropatterns were produced by replica molding in silicone. The adhesion forces were characterized systematically by means of experiments and numerical modeling. The force increased with the square of the applied voltage for electric fields up to 800 V. For larger fields, a less-than-quadratic scaling was observed, which is likely due to the small, field-dependent electrical conductivity of the materials involved. The additional adhesion force was found to be up to twice of the field-free adhesion. The results suggest an alternative method for the controlled handling of fragile or miniaturized objects.

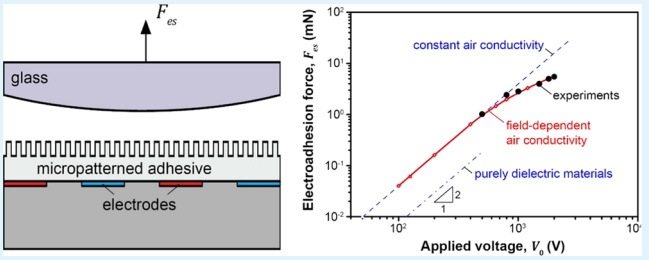

KEYWORDS: *micropatterned adhesives, electroadhesion, microhandling, air conductivity, Maxwell stresses*

1. INTRODUCTION

Temporary adhesive contacts between solid bodies can be achieved using various techniques and promote attractive alternatives to mechanical grippers for continuous automatic handling and assembly. To date, vacuum grippers are widely used in pick-and-place applications with high precision in positioning.[1] Mechanical, magnetic, and electromagnetic grippers offer alternatives to specific applications but are used less frequently. A novel approach is the utilization of micropatterned adhesives.[2−5] Their performance relies mainly on van der Waals interactions and contact mechanics, which are controlled by mechanical properties and the proper design and arrangement of the microstructures in an adhesive array.[6−8]

Pick-and-place applications necessitate a controllable switch between a high (pick) and a low (release) adhesive regime. Several examples of external stimuli for switching adhesion of micropatterned adhesives have been reported, including compressive loads,[9,10] heating,[11,12] magnetic fields,[13,14] pneumatic control,[5,15] and UV exposure.[16] Almost all mentioned strategies require specific designs or material selection, which potentially limit the range of applications. In addition, most concepts allow switching between "on" and "off" states but no specific adjustability to the required adhesion performance.

An approach to control adhesion during operation is electroadhesion. Electroadhesion functions for both conductive and insulating targets[17−19] and is, for example, used in semiconductor wafer handling[20] or microhandling.[21] Electroadhesion devices typically make use of interdigitated electrode arrays to maximize the spatial extent of regions with high electric field strengths and high field gradients.[18] The traditional electrostatic models predict a dependence of the electroadhesion force on the square of the applied voltage difference.[22] Recently, electroadhesion has been combined with micropatterned adhesives for applications such as wall climbing robots[23] and flexible grippers.[24] Spenko et al. and Menon et al. have successfully demonstrated that the combination of both concepts improves shear adhesion, as the normal force induced by electrical fringe fields forces closer contact with higher friction.[25,26]

The objective of the present paper is to study the influence of superimposed electroadhesion on the normal adhesion of polymeric micropatterns. The details of the experimental setup and the electroadhesion device fabrication are described in Section 2, and the experimental results are provided in Section 3. A description of the theoretical models both for electrically insulating and electrically conductive materials is given in Section 4, followed by an in-depth numerical evaluation of the models and a comparison with the experimental data in Section 5.

Received: March 18, 2020
Accepted: May 21, 2020
Published: May 21, 2020

https://dx.doi.org/10.1021/acsami.0c05077
ACS Appl. Mater. Interfaces 2020, 12, 27708−27716

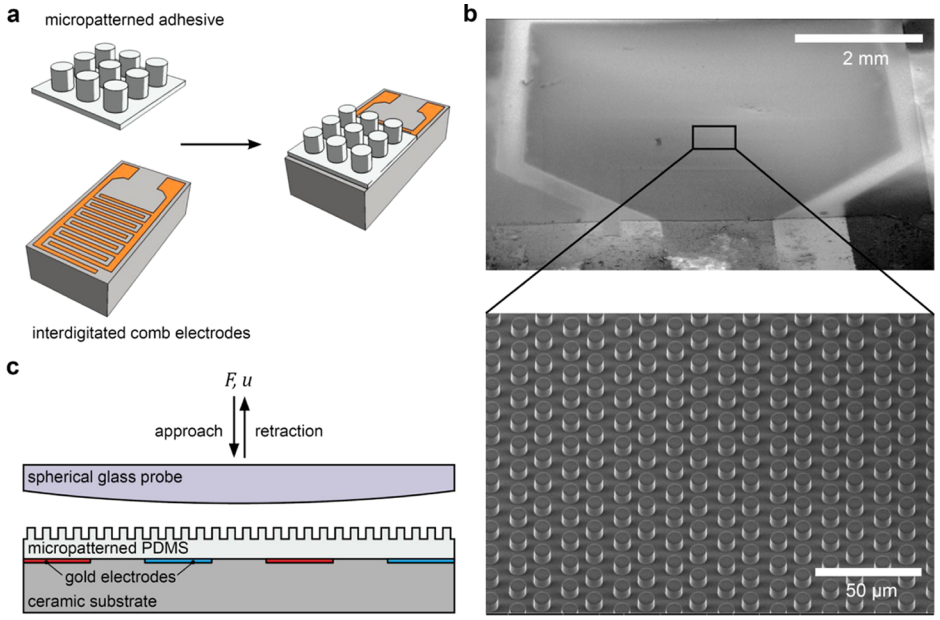

Figure 1. Micropatterned electroadhesive device. (a) Illustration of the basic setup. A micropatterned adhesive film was generated via replica molding and, subsequently, deposited on the interdigitated comb electrodes. (b) Scanning electron micrograph of the micropatterned electroadhesive device. The inset shows the micropillars. (c) Schematic of the adhesion test setup. During the test, a spherical glass probe was attached (approach) and detached (retraction) at different applied voltages. Normal forces F and displacements u were recorded.

2. MATERIALS AND METHODS

2.1. Device Fabrication. For the micropatterned electroadhesive device, micropatterned polymeric films were transferred onto interdigitated comb electrodes. The micropatterns consisted of cylindrical pillars with a diameter and height of 7 μm (aspect ratio 1:1). The fabrication included three replication steps. In the first step, a lithographically patterned silicon wafer with holes (negative master template) was replicated using poly(dimethylsiloxane) (PDMS, Sylgard 184, Dow Corning, Midland, MI). PDMS was prepared by mixing ten parts of the base material with one part of the curing agent using a speed mixer (DAC600.2 VAC-P, Hauschild Engineering, Hamm, Germany) at 2350 rpm for 3 min. In the second step, a replica structure made of UV-curable perfluoropoly(ether-dimethacrylate) (Fomblin MD40, Solvay, Bollate, Italy) was obtained. The prepolymer contained 0.5 wt % of a photoinitiator (2-hydroxy-2-methyl-propiophenone, Sigma-Aldrich, Taufkirchen, Germany). The mixture was poured over the first PDMS template and covered with a microscope glass slide. The prepolymer mixture was exposed to UV (wavelength 365 nm, Omnicure S1500, Excelitas Technologies) in a nitrogen atmosphere for 5 min. The cured structure was carefully peeled and served as a template (negative) for the fabrication of the micropatterned adhesive films made from poly(dimethylsiloxane) (PDMS, Sylgard 184, Dow Corning, Midland, MI). PDMS was prepared as described above. The mixture was poured over the MD40 template and covered with interdigitated electrodes (IDEAU200, Deutsche METROHM GmbH & Co. KG, Filderstadt, Germany). Prior to this, the electrodes were treated with oxygen plasma for 3 min to promote the adhesion of the silicone film to the electrode surface. Electrodes had a width of 220 μm and a gap between oppositely charged electrodes of 160 μm. A fixture was used to clamp the template, the electrodes, and the intermediate liquid PDMS layer to set the desired backing layer thickness of the micropatterned film. The whole setup was placed in an oven, thermally cured at 95 °C for 20 min, and finally demolded.

The micropatterned electroadhesive device was fabricated by combining an elastomeric micropatterned film with an interdigitated comb electrode array, as shown in Figure 1. The diameter and height of the micropillars were 7 μm. The pillars were arranged hexagonally with a center-to-center distance of 14 μm, which is one order of magnitude smaller compared to the width (220 μm) and distance (160 μm) between the electrodes. The backing layer was 55 ± 5 μm, which is one order of magnitude larger than the pillar height. Thus, we assume that the characteristics of the electrical fringe field were not influenced by the spatial orientation of the pillar array in relation to the direction of the electrodes.

2.2. Electroadhesion Setup. The normal adhesion was characterized using a custom-built setup. A spherical glass lens with a curvature radius of 15.5 mm (Edmund Optics GmbH, Mainz, Germany) was used as a probe. The probe was mounted on a load cell (KD 34s ME-Meßsysteme, Hennigsdorf, Germany) to measure normal forces. The probe and load cell were displaced using a linear stage (Q-545 Q-Motion, Physik Instrumente GmbH & Co. KG, Karlsruhe, Germany). The micropatterned electroadhesive device was mounted below the probe and connected to a DC high-voltage power supply (HCN 14-3500, FuG Electronik GmbH, Schechen, Germany). A LabVIEW program was developed to control the electroadhesion setup. To reduce residual charges in adhesion measurements in the presence of an electrical field, the probe and adhesive film were treated by an antistatic gun upon each measurement (Zerostat 3 Anti-Static, SPI Supplies, Glasgow, U.K.). All experiments were performed in a laboratory with controlled temperature and relative humidity (RH) at 21 °C and 50 ± 5%, respectively.

During the approach, the spherical probe was brought in contact with the adhesive film. At the maximum indentation depth, the compressive preload was the highest. This position was held for 1 s, before the probe was retracted. In all experiments, the approach and retraction velocities were 1 μm/s. The displacement of the probe, u, was calculated as follows: $u = u_M - F/k$, where u_M is the displacement of the motorized stage, F is the force, and k = 6.17 kN/m is the machine stiffness. The absolute value of the maximum adhesive force at detachment was defined as the pull-off force. The pull-off forces were converted into pull-off stresses by dividing them with the projected contact area, A_p, at the maximum compressive preload. The projected contact area was calculated by the geometrical formula $A_p = \pi(R^2 - (R - u_p)^2)$, where R = 15.5 mm is the curvature radius of the probe and u_p is the distance from the contact to maximum indentation of the probe into the micropatterned film.

https://dx.doi.org/10.1021/acsami.0c05077
ACS Appl. Mater. Interfaces 2020, 12, 27708−27716

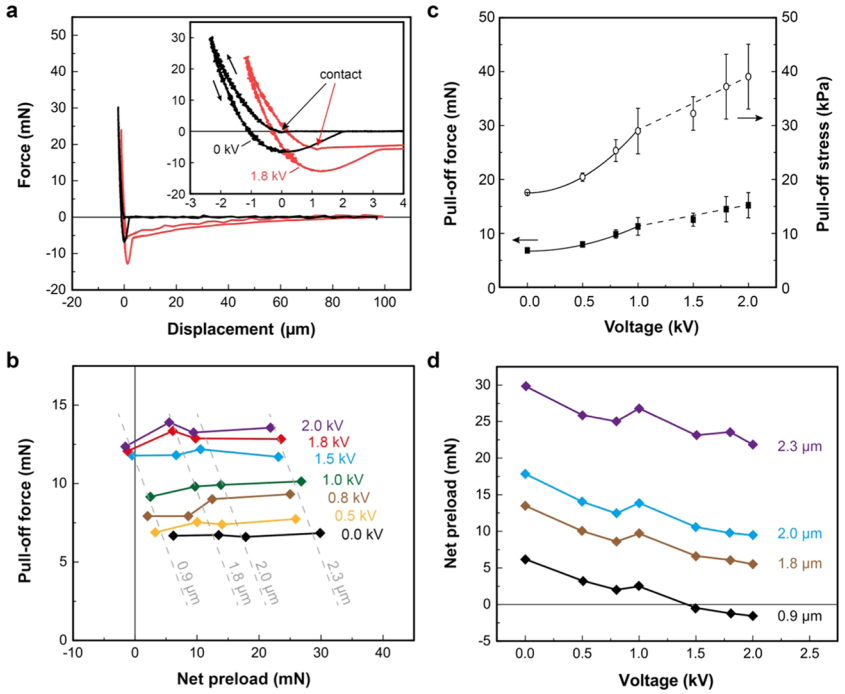

Figure 2. Electroadhesion results. (a) Force−displacement curves for 0 kV (black) and 1.8 kV (red). The positive and negative forces are compressive and tensile forces, respectively. The inset presents data close to the contact of the probe with the micropatterned adhesive film. The arrows indicate the path during approach and retraction. (b) Pull-off forces in terms of net preloads for various applied voltages. The dashed lines highlight data for constant indentations. (c) Pull-off force (solid squares) and pull-off stress (open circles) as a function of the applied voltage. The solid and the dashed lines illustrate quadratic and linear functions, respectively. (d) Net preload as a function of the applied voltage. The numbers represent the indentation into the micropatterned adhesive.

3. EXPERIMENTAL RESULTS

The results of adhesion tests for different applied voltages are shown in Figure 2. Figure 2a compares the results with (1.8 kV) and without (0 kV) the applied electrical field. Without the applied field (black curve), the normal force was zero before the probe contacted the micropatterned surface ($u \geq 0$ μm). The contact was established by pressing the probe into the adhesive film (indentation) up to a preset displacement of −2.3 μm. In that position, the maximum compressive preload of 30 mN was achieved. Upon holding for 1 s, the probe was retracted. The probe detached from the surface at a maximum tensile force of −7 mN, i.e., a pull-off force of 7 mN. This pull-off force must be attributed to van der Waals interactions.

In the presence of an electrical field (red curve), the probe already experienced an attractive force before contact (for $u \lesssim 70$ μm). At contact, the attractive force due to the electrical field was −5 mN. The maximum compressive preload reduced apparently to 25 mN for a similar indentation of −2.3 μm in relation to the experiment without the electrical field. The attractive electrostatic force further caused earlier contact at u = 1.1 μm. This effect is related to the elastically deformable setup with a machine stiffness of 6.17 kN/m and constant motor displacement for all measurements. The pull-off force was 12 mN. Upon detachment, the force gradually decreased with increasing distance between the probe and the adhesive, similar to the approach. The slightly higher attractive force (about 1 mN) during retraction compared to the approach is most likely related to residual charges upon separation of contact.

Figure 2b shows the pull-off force as a function of the net preload (i.e., the sum of the negative, compressive mechanical preload, and the positive, attractive electroadhesion) for various applied voltages. The pull-off forces increased with the applied voltage and at 2 kV were twice as high as at 0 kV. With increasing voltage, the net preload decreased for constant displacements due to increasing electrostatic attraction between the adhesive and the probe. Although the probe was spherical, pull-off forces were insensitive to preload, as all measurements were performed in saturation conditions, i.e., the pull-off force was insensitive to preload.[27] Figure 2c summarizes the pull-off forces in terms of applied voltages. Pull-off forces and stresses increased with increasing electric fields, which suggests that the electrostatic forces superimpose on van der Waals forces. Compared to the field-free case, a typical enhancement of adhesion by factor 2 was achieved at a voltage of 2 kV. It is notable that the adhesion force or stress appeared to increase parabolically, as expected theoretically, only up to about 800 V; above this value, an approximately linear relationship with applied voltage was found.

Importantly, the electrostatic force contributed to the contact formation of the probe with the adhesive, which led to a reduced net preload, although the displacement from the first contact to maximum indentation was kept constant. Thus, the net preload reduced with increasing voltage, as shown in Figure 2d. For small indentations such as 0.9 μm, the net preload turned negative for voltages larger than 1.5 kV. Here, the requisite compressive force of the probe to adhere to the surface was realized solely by electrostatic forces without mechanical compression.

4. THEORETICAL MODELS

The experimental results suggest that the achievable adhesion force was enhanced by a switchable electric field-induced force exerted on the probe. Below, we present the theoretical models for different types of materials as well as their numerical implementation to predict the steady-state values of the electroadhesion force. The boundary conditions are introduced in Section 4.6. We used finite-element software Comsol 5.2.

4.1. Electrostatic Interaction—Insulating Materials. We first consider a stationary electrostatic system that is composed of purely dielectric, i.e., electrically insulating, materials. The electric field distribution is governed by Poisson's equation

$$\nabla\cdot(\varepsilon_0\varepsilon_r\nabla V) = -\rho \quad (1)$$

https://dx.doi.org/10.1021/acsami.0c05077
ACS Appl. Mater. Interfaces 2020, 12, 27708−27716

where ε_r is the relative permittivity of the respective material, ε_0 is the vacuum permittivity, V is the electric potential, and ρ is the volume charge density. We assume the dielectric materials to be linear, nondissipative, isotropic, and homogeneous. We assume all material properties to be independent of elastic deformations. Moreover, we assume all surface and volume charge densities to be zero, except on the surface of the electrodes in all simulations pertaining to this section. The electrical potential is continuous at all interfaces, which implies the continuity of the tangential component of the electric field vector. The normal component of the electric field vector is discontinuous at the interface between two materials a and b according to

$$\mathbf{n}\cdot(\varepsilon^a\mathbf{E}^a - \varepsilon^b\mathbf{E}^b) = 0 \tag{2}$$

where $\mathbf{n}$ is the unit normal vector of the interface pointing from material a to material b and $\mathbf{E}$ is the electric field vector.

4.2. Bulk-Conductive Materials. We now consider all materials to have a nonzero electrical bulk conductivity σ. This is motivated by the fact that, in the experiments, the electric field strength is comparable to or even above the dielectric breakdown strength of air of approximately 3 MV/m. At such high electric fields, many materials that are normally considered electrically insulating actually behave as weak conductors. This applies to air, elastomer, and possibly also glass.[28−30]

Assuming no external currents, we solve the continuity equation in steady state

$$\nabla\cdot\mathbf{J} = 0 \tag{3}$$

where according to Ohm's law the bulk current density is given by $\mathbf{J} = \sigma\mathbf{E}$. Eq 3 is equivalent to

$$\nabla\cdot(-\sigma\nabla V) = 0 \tag{4}$$

We assume σ to be homogeneous in all materials except air, where we consider the conductivity to be dependent on the local electric field, as discussed in Section 4.4. The electrical potential is continuous at all interfaces. The normal component of the electric field vector is discontinuous at the interface between two materials a and b according to

$$\mathbf{n}\cdot(\sigma^a\mathbf{E}^a - \sigma^b\mathbf{E}^b) = 0 \tag{5}$$

which represents the continuity of the normal component of the bulk current density.

4.3. Surface Conductivity of Glass−Air Interfaces. In our experiments, we used glass lenses as probes. The electrical bulk conductivity of glass at room temperature is almost unmeasurably small, i.e., essentially zero.[31] However, there is a significant electrical surface conductivity due to moisture adsorption that must be taken into account.[32−35]

The surface conductivity is implemented by assuming an ultralow bulk conductivity of the lens (10^{-30} S/m) and an additional interfacial condition at the glass−air interface

$$\mathbf{n}\cdot(\mathbf{J}^{\text{glass}} - \mathbf{J}^{\text{air}}) = \mathbf{n}\cdot(\sigma^{\text{glass}}\mathbf{E}^{\text{glass}} - \sigma^{\text{air}}\mathbf{E}^{\text{air}}) = -\nabla_s\cdot\mathbf{j}_s \tag{6}$$

where ∇_s is the surface gradient operator and $\boldsymbol{n}$ is the unit normal vector of the interface pointing from glass to air.[36−38] Eq 6 represents charge conservation across the glass−air interface and relates a discontinuity in the bulk current density to the surface divergence of the surface current density $\mathbf{j}_s = \sigma_s\nabla_s V$, where σ_s is the surface conductivity. At all other interfaces, eq 5 holds. The electrical potential is continuous at all interfaces.

4.4. Variable Air Conductivity. At very high electric fields approaching the dielectric breakdown limit, the electrical conductivity of air σ_{air} is dependent on the electric field strength. Carlon has measured the electrical conductivity of air at very high relative humidities RH ≥ 66%.[39] It was found that σ_{air} was constant for low fields and increased rapidly for $|\mathbf{E}|$ exceeding a certain threshold value E_c. The blue symbols in Figure 3 are extracted from his measurements for RH = 66%.

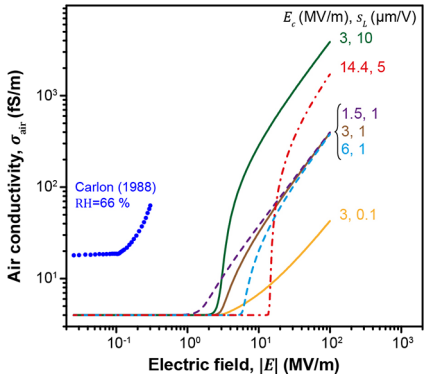

Figure 3. Models for the electric field dependence of the air conductivity (see eq 7). The solid lines vary the slope s_L for threshold value E_c = 3 MV/m, and the dashed lines vary E_c for s_L = 1 μm/V. The dash-dotted red line was found to match experimental results with E_c = 14.4 MV/m and s_L = 5 μm/V. The blue symbols are extracted from measurements of Carlon for moist air (RH = 66%).[39]

In this case, E_c is approximately 0.1 MV/m, which is substantially lower than the breakdown strength. He also observed very strong humidity dependence of the low field conductivity. Several groups reported low field conductivities of air between 1 and 100 fS/m, depending on the geographic location, air pollution, and atmospheric conditions.[28,29,40,41] Because quantitative measurements of field-dependent conductivity are scarce, we use the following empirical relation

$$\frac{\sigma_{\text{air}}}{\sigma_0} = 1 + s_L E_0 \log\left[1 + \exp\left(\frac{|\mathbf{E}| - E_c}{E_0}\right)\right] \tag{7}$$

where σ_0 is the zero-field air conductivity, E_c is the critical field strength below which the conductivity is constant and above which it increases, E_0 = 0.1 MV/m defines the width of the transition region, and s_L defines the slope. The curves of $\sigma_{\text{air}}(E)$ for different values of E_c and s_L are illustrated in Figure 3. We assume σ_0 = 4 fS/m as the standard laboratory conditions usually correspond to relatively dry air (RH 30−40%).[28] It is seen that the empirical relation gives a smooth transition between the constant and linear regimes.

4.5. Electroadhesion Force. The electroadhesion force F_{es} acting on a target object in a nonuniform electric field is derived from the Maxwell stress tensor T_{ij}, given as

$$T_{ij} = D_i E_j - \frac{1}{2}\delta_{ij}\sum_{k=1}^{3} D_k E_k \tag{8}$$

where $E_i \equiv -\partial V/\partial x_i$ is the electric field, $D_i \equiv \varepsilon_0\varepsilon_r E_i$ is the electric displacement field, and δ_{ij} is the Kronecker delta. At a boundary between two materials of different permittivities such

https://dx.doi.org/10.1021/acsami.0c05077
ACS Appl. Mater. Interfaces 2020, 12, 27708−27716

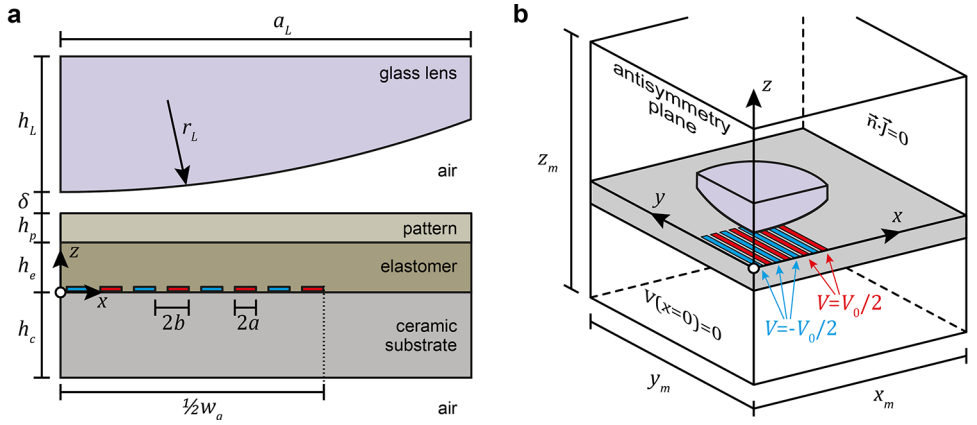

Figure 4. Schematic illustration of the computational model. (a) Cross section (y = 0 plane) of the glass lens (purple, curvature radius r_L) placed above oppositely charged electrodes (red and blue stripes) located on a ceramic substrate (gray). The electrode array is covered with a thin elastomer layer with thickness h_e. The patterned surface is approximated by a thin homogeneous effective medium layer with thickness h_p. (b) In the simulations, a cuboidal quarter of the experimental setup is considered, with a symmetry plane at y = 0 and an antisymmetry plane at x = 0.

Table 1. List of Variables as well as Geometric and Material Parameters Used in the Numerical Simulations

material	property	symbol	value	unit	reference
air	relative permittivity	ε_{air}	1		
	conductivity	σ_{air}	4×10^{-15}	S/m	28
	gap thickness	δ	1×10^{-6}	m	
lens	relative permittivity	ε_L	5		42
	conductivity	σ_L	10^{-12}	S/m	
	surface conductivity	σ_s	10^{-13}– 10^{-8}	S	43, 44
	radius	a_L	8×10^{-3}	m	
	radius of curvature	r_L	0.0155	m	
	thickness	h_L	4×10^{-3}	m	
pattern	pillar radius	r_p	3.5×10^{-6}	m	
	pillar height	h_p	7×10^{-6}	m	
	pillar spacing	s_p	1.4×10^{-5}	m	
elastomer	relative permittivity	ε_e	2.5		30
	conductivity	σ_e	2.5×10^{-14}	S/m	30
	thickness	h_e	5.5×10^{-5}	m	
electrode array	electrode half-width	a	1.1×10^{-4}	m	
	half-period	b	1.9×10^{-4}	m	
	number of electrodes	n	16		
	applied voltage	V_0	2000	V	
ceramic substrate	relative permittivity	ε_c	10		45
	conductivity	σ_c	10^{-13}	S/m	46
	thickness	h_c	3×10^{-3}	m	
computational domain	width, length	x_m, y_m	0.02	m	
	height	z_m	0.04	m	

as glass and air, the stress tensor T_{ij} is discontinuous, which causes a mechanical force density S_i to act on the boundary

$$S_i = (T_{ij}^{air} - T_{ij}^{glass})n_j \quad (9)$$

The Maxwell stress vector S_i represents the electromechanical coupling. The total electroadhesion force is calculated by integrating S_z over the surface area A of the lens

$$F_{es} = \oiint S_z dA \quad (10)$$

4.6. Computational Domains, Boundary Conditions, and Material Properties. Figure 4 shows the model geometry. A glass lens is positioned above the electrode array. The width and length of the electrode array are $w_a = 2b(n-1) + 2a$ with n interdigitated stripe electrodes of width $2a$ and period $2b$ (Figure 4a). The electrode array is deposited on a ceramic substrate with thickness h_c = 3 mm, relative permittivity ε_r = 10, and conductivity σ = 100 fS/m. The array is covered with an elastomer layer of thickness h_e = 55 μm, relative permittivity ε_e = 2.5, and conductivity σ_e = 25 fS/m. The elastomer is covered with a hexagonal array of cylindrical micropillars. As the pillars are too small to be considered individually, we use an effective medium approximation. The effective medium has a thickness equal to the pillar height h_p = 7 μm. Its permittivity and conductance are derived from those of the elastomer and air and equal $\varphi\varepsilon_e + (1-\varphi)\varepsilon_{air} \approx 1.34$ and $\varphi\sigma_e + (1-\varphi)\sigma_{air} \approx 8.76$ fS/m, where $\varphi = \frac{\pi\sqrt{3}}{6}\left(\frac{2r_p}{s_p}\right)^2 \approx 0.227$ is the volume filling ratio of the pillar array, r_p = 3.5 μm is the pillar radius, and s_p = 14 μm is the spacing of the pillars. The glass lens has a relative

https://dx.doi.org/10.1021/acsami.0c05077
ACS Appl. Mater. Interfaces 2020, 12, 27708−27716

permittivity $\varepsilon_L = 5$, conductivity $\sigma_L = 1$ pS/m, radius of curvature $r_L = 15.5$ mm, diameter $2a_L = 16$ mm, and thickness $h_L = 4$ mm and is placed $\delta = 1$ μm (unless specified otherwise) above the pattern. Air is assumed to have a relative permittivity of 1 and conductivity $\sigma_{air} = 4$ fS/m at zero field strength. All geometric and material parameters are summarized in Table 1.

Due to symmetry, we only consider a cuboidal quarter of the system with width $x_m = 20$ mm, length $y_m = 20$ mm, and height $z_m = 40$ mm. The glass lens is positioned above the electrode array (Figure 4b). A quarter of the electrode array has width and length $w_a/2 = 3$ mm and is composed of $n = 8$ electrodes of width $2a = 220$ μm and period $2b = 380$ μm. At $y = 0$, there is a symmetry plane where $\mathbf{n}\cdot\mathbf{E} = 0$ and $\mathbf{n}\cdot\mathbf{J} = 0$ hold. At $x = 0$, there is an antisymmetry plane where $V = 0$ holds. All other external boundaries are also considered to be symmetry planes and positioned distant enough (i.e., $x_m, y_m, z_m \gg w_a/2$) to have no influence on the solution.

5. NUMERICAL RESULTS

Figure 5 shows an example of the Maxwell stress distribution $|S_z|$ on the lower surface of the lens. Faint white lines indicate

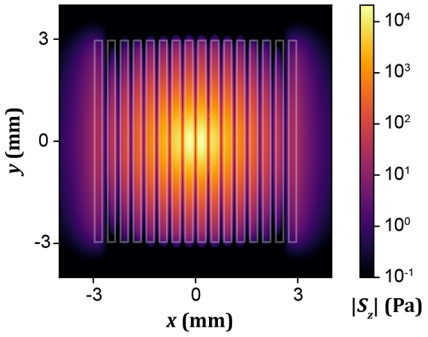

Figure 5. Distribution of electroadhesion stress: logarithmic Maxwell stress map on the surface of the lens located 1 μm above the micropatterned electroadhesive device. The white lines indicate the shape and location of the electrode array.

the position of the electrode array. Most of the attraction is concentrated directly above each electrode and near the center of the lens being located 1 μm above the micropatterned adhesive. The outermost electrodes exhibit a weak long-range attraction due to fringe fields.

Figure 6 shows the extracted electroadhesion force F_{es} acting on the lens in terms of the applied voltage, as evaluated using eq 10. The black circles represent our experimental measurements. The dashed and dash-dotted black lines, both scaling as $F_{es} \sim V_0^2$, correspond to the constant air conductivity and the electrostatic model for insulating materials, respectively. It matches the experimental data well up to 800 V. Above that voltage, the experiments no longer follow the quadratic force–voltage dependence predicted by this model. Other symbols in Figure 6 correspond to a field-dependent air conductivity according to eq 7. The electroadhesion force is proportional to V_0^2 for low voltages but exhibits a weaker scaling when $E > E_c$. The best fit is obtained for parameter values $E_c = 14.4$ MV/m and $s_L = 5$ μm/V (red line). A comparison of the data for $E_c = 3$ MV/m and $s_L = 0.1$ and 10 μm/V (orange and blue lines) illustrates that a larger value of s_L induces a weaker dependence of F_{es} on V_0 for $E \gg E_c$. Variations of E_c (green and violet lines) determine at which voltage level the deviation from the square scaling occurs.

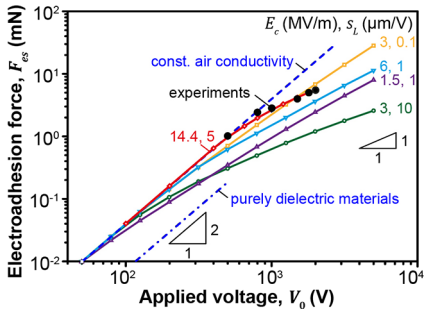

Figure 6. Numerical results of electroadhesion force as a function of the applied voltage: the variable air conductivity was calculated according to eq 7 with threshold value E_c and slope s_L (compare Figure 3). The black circles represent experimental results. The dashed black line assumes a constant air conductivity. The dash-dotted black line corresponds to the electrostatic model.

A comparison of the models introduced in Section 4 and specifically the effect of air conductivity and electric parameters are shown in Figure 7. First, the influence of the field-independent surface conductivity of the lens σ_s (blue crosses) and the field-independent bulk conductivity of the lens σ_L (orange diamonds) on the electroadhesion force F_{es} is displayed in Figure 7a. In both cases, F_{es} increases for a more conductive lens. It approaches a constant value for large σ_L because the lens behaves as a perfect conductor and the interior electric field vanishes. Similarly, in the limit of small σ_L, the force approaches a constant value, as the lens becomes a perfect insulator. The force changes sign because better conductors than air tend to be attracted to and poorer conductors than air repelled from regions with high electric fields. We conclude that the two models give virtually identical results if the value of σ_s is chosen as $\sigma_s = \lambda\sigma_L$, where $\lambda \approx 122$ μm for our system. The line represents a fit based on the function

$$F_{es}(\sigma) = c_0 + \frac{c_1}{1 + \frac{c_2}{\sigma}} \tag{11}$$

where c_0, c_1, and c_2 are fit parameters. The dashed vertical line corresponds to the (field-independent) air conductivity σ_{air}. When $\sigma_L = \sigma_{air}$, the force crosses zero. For a lower computational cost, the bulk conductivity model was chosen in further calculations, although the surface conductivity model was more physically relevant.

In Figure 7b, we show the dependence of F_{es} on the (field-independent) conductivity of air σ_{air} (red points) and the elastomer σ_e (violet squares). F_{es} decreases with increasing σ_{air}. Consequently, if σ_{air} increases with field strength, the force will be lower. F_{es} substantially increases with increasing σ_e, because the high-field region extends closer to the air–lens interface. This can provide an additional parameter for tuning the performance of electroadhesion devices. F_{es} approaches zero in the limits of $\sigma_{air} \gg \sigma_e$, because a large air conductivity prevents any appreciable electric field strength from reaching the air–lens interface. For the same reason, F_{es} approaches zero in the limit $\sigma_e \to 0$. Figure 7c displays the increase of F_{es} with increasing relative permittivities of the lens ε_L and the elastomer ε_e for purely dielectric materials. The electroadhesion force scales linearly with $\varepsilon_L - 1$ for small ε_L and approaches a constant value for large ε_L. A scaling argument explaining these limiting behaviors is presented in Section S5 in the Supporting Information. Figure 7d shows F_{es} as a

https://dx.doi.org/10.1021/acsami.0c05077
ACS Appl. Mater. Interfaces 2020, 12, 27708–27716

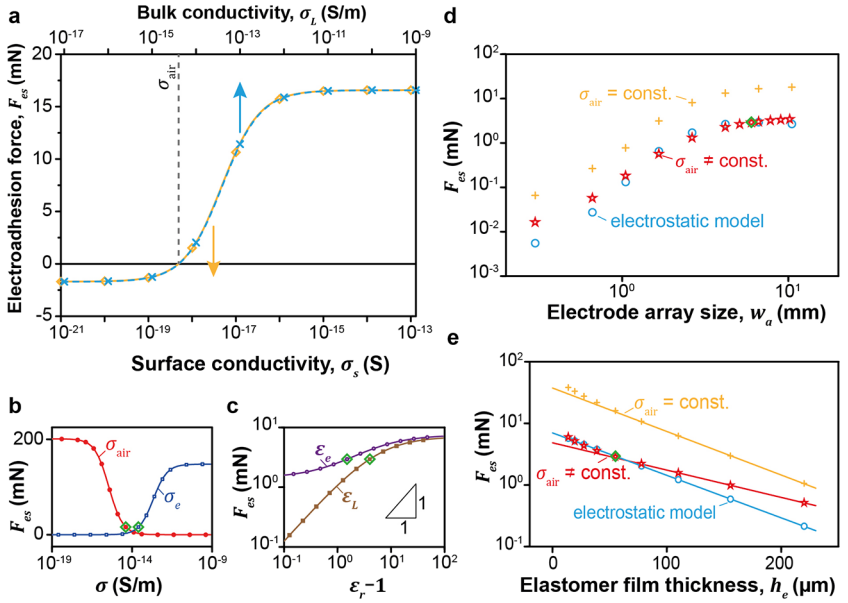

Figure 7. Comparison of numerical models and effect of air conductivity and electric parameters on electroadhesive force F_{es}. (a) Comparison of the surface and bulk conductivity models: F_{es} in terms of the field-independent surface (σ_s, blue crosses) or bulk (σ, orange diamonds) conductivity of the lens. The solid blue and red dashed lines are fits based on the logistic function, compare eq 11. In the bulk conductivity model, the fitted function crosses zero force for a lens conductivity equal to that of air (dashed gray line). (b) Electroadhesive force as a function of the air conductivity (σ_{air}, red circles) and elastomer conductivity (σ_e, blue squares). (c) Electroadhesive force as a function of the lens permittivity (ε_L, brown squares) and elastomer permittivity (ε_e, violet circles) assuming purely dielectric materials. (d, e) Electroadhesive force in terms of (d) size of the electrode array w_a and (e) thickness of the elastomer film h_e for linearly varying air conductivity (red stars, E_c = 3 MV/m and s_L = 1 μm/V) and field-independent air conductivity (orange pluses) and in the electrostatic model (blue circles). The lines in (e) represent exponential fits to the three thickest films of each data set. As a reference, the green diamonds in (b−e) represent the parameter values stated in Table 1.

function of the entire electrode array width and length w_a while keeping the number of electrodes and the ratio a/b constant. The electroadhesion force increases with larger w_a. For w_a > 5 mm, the force approaches saturation as the array is much larger than the region of low separation and high attraction due to the curvature of the lens (compare Figure 5). Figure 7e illustrates how F_{es} varies with elastomer thickness h_e. For a large thickness, this relation is exponential as illustrated by exponential fits (solid lines), because the potential due to the coplanar interdigitated electrode arrays decays exponentially in the direction normal to the substrate.[47] For small separation, the extracted force is higher than the long-range exponential fit. The dependence of the force on electrode width−period ratio a/b is given in Section S1 in the Supporting Information.

6. DISCUSSION

We have fabricated and evaluated a micropatterned electroadhesion device based on an interdigitated electrode and a polymer micropillar array. Attractive forces before and after contact were caused by long-range electrostatic forces, while during contact, the short-range van der Waals forces additionally contribute to adhesion. The traditional theoretical models for electroadhesion consider purely dielectric materials, i.e., electrical insulators, for which the electroadhesion force scales quadratically with applied voltage. This is in contrast to our experimental results as well as previous ones reported in the literature,[48−50] where a weaker force−voltage scaling has been observed for voltages above 800 V. We have shown that accounting for the minute but finite electric field-dependent electrical conductivities of air and the solid materials used in the device can quantitatively reproduce the experimental results.

The conductivities of the typical materials involved in an electroadhesion device can vary vastly. The surface conductivity of glass can change by seven orders of magnitude depending on the relative humidity and is sensitive to surface contamination e.g., due to fingerprints or residues upon repeated attachment and detachment cycles.[51] The bulk conductivity of polymers can vary strongly depending on the impurity concentrations and production methods. Moreover, the conductivity of air depends on the relative humidity and the geographic microlocation of the measurement. Guo et al. reported a drop in the electroadhesion force exerted on a glass target substrate by approximately a factor of 3 over the course of 3 days when the relative humidity decreased from approximately 64 to 43%.[18] This is qualitatively consistent with the variation observed in Figure 7a. These results and considerations point at the need for tightly controlled environmental parameters to achieve a stable and reproducible electroadhesion performance.

In terms of potential applications, the findings of this study offer an opportunity for novel pick-and-place devices: by combining the adhesion of a micropatterned polymer with electrostatic interaction, very fragile objects could be handled without applying mechanical compression. Electric fields could also be used to enhance adhesion to objects with rough surfaces, where van der Waals interactions are insufficient.[19]

7. CONCLUSIONS

Our experimental and numerical approach successfully revealed how short-range van der Waals interactions can be superimposed by long-range electrostatic forces, which enables in-line regulation of preload and adhesion forces. The following conclusions can be drawn:

https://dx.doi.org/10.1021/acsami.0c05077
ACS Appl. Mater. Interfaces 2020, 12, 27708−27716

- The presence of electrostatic fields enhances adhesion. Compared to the field-free case, an enhancement of adhesion by about a factor 2 (at a voltage of 2 kV) was achieved.
- Up to 800 V, the adhesion force scaled with the square of the applied voltage. For voltages larger 800 V, the scaling was weaker; this effect is very likely due to the small, field-dependent electrical conductivity of the materials involved.
- The numerical results were similar for bulk-conductive materials and a model presuming the surface conductivity of glass−air interfaces. The latter has physical relevance due to the possible adsorbed water films or residues through repeated adherence and detachment cycles.
- The electrical adhesive force could be further increased by decreasing the thickness of the micropatterned polymer or by increasing the permittivity and conductivity of the elastomer material. The numerical results also indicate that the electroadhesive force is highly sensitive to the environmental conditions; in particular, the force is predicted to decrease with increasing air conductivity, which is directly related to humidity.

■ ASSOCIATED CONTENT

Supporting Information

The Supporting Information is available free of charge at https://pubs.acs.org/doi/10.1021/acsami.0c05077.

Dependence of the electroadhesion force on the a/b ratio, model validation for flat surfaces, validation of the effective medium approximation, comparison between idealized and realistic geometries of the electrode array, and scaling of the Maxwell traction for purely dielectric materials (PDF)

■ AUTHOR INFORMATION

Corresponding Author

Eduard Arzt − *INM—Leibniz Institute for New Materials, 66123 Saarbrücken, Germany; Department of Materials Science and Engineering, Saarland University, 66123 Saarbrücken, Germany*; Email: eduard.arzt@leibniz-inm.de

Authors

Vaishali Chopra − *INM—Leibniz Institute for New Materials, 66123 Saarbrücken, Germany; Department of Materials Science and Engineering, Saarland University, 66123 Saarbrücken, Germany*

Maciej Chudak − *Department of Applied Physics, Eindhoven University of Technology, 5600 MB Eindhoven, Netherlands*

René Hensel − *INM—Leibniz Institute for New Materials, 66123 Saarbrücken, Germany*; orcid.org/0000-0002-9623-2118

Anton A. Darhuber − *Department of Applied Physics, Eindhoven University of Technology, 5600 MB Eindhoven, Netherlands*; orcid.org/0000-0001-8846-5555

Complete contact information is available at: https://pubs.acs.org/10.1021/acsami.0c05077

Notes

The authors declare no competing financial interest.

■ ACKNOWLEDGMENTS

The research leading to these results was funded through the European Union's Horizon 2020 Research and Innovation Program under the Marie Skłodowska-Curie grant agreement no. 642861.

■ REFERENCES

(1) Hollis, R. L.; Gowdy, J.; Rizzi, A. A. Design and Development of a Tabletop Precision Assembly System. *Mechatronics Rob.* **2004**, 1619−1623.

(2) Zhou, M.; Tian, Y.; Sameoto, D.; Zhang, X.; Meng, Y.; Wen, S. Controllable Interfacial Adhesion Applied to Transfer Light and Fragile Objects by Using Gecko Inspired Mushroom-Shaped Pillar Surface. *ACS Appl. Mater. Interfaces* **2013**, *5*, 10137−10144.

(3) Jeong, H. E.; Lee, J.-K.; Kim, H. N.; Moon, S. H.; Suh, K. Y. A Nontransferring Dry Adhesive with Hierarchical Polymer Nanohairs. *Proc. Natl. Acad. Sci. U.S.A.* **2009**, *106*, 5639−5644.

(4) Purtov, J.; Frensemeier, M.; Kroner, E. Switchable Adhesion in Vacuum Using Bio-Inspired Dry Adhesives. *ACS Appl. Mater. Interfaces* **2015**, *7*, 24127−24135.

(5) Song, S.; Drotlef, D.-M.; Majidi, C.; Sitti, M. Controllable Load Sharing for Soft Adhesive Interfaces on Three-Dimensional Surfaces. *Proc. Natl. Acad. Sci. U.S.A.* **2017**, *114*, E4344−E4353.

(6) Hensel, R.; Moh, K.; Arzt, E. Engineering Micropatterned Dry Adhesives: From Contact Theory to Handling Applications. *Adv. Funct. Mater.* **2018**, *28*, No. 1800865.

(7) Booth, J. A.; Tinnemann, V.; Hensel, R.; Arzt, E.; McMeeking, R. M.; Foster, K. L. Statistical Properties of Defect-Dependent Detachment Strength in Bioinspired Dry Adhesives. *J. R. Soc., Interface* **2019**, *16*, No. 20190239.

(8) Tinnemann, V.; Hernández, L.; Fischer, S. C. L.; Arzt, E.; Bennewitz, R.; Hensel, R. In Situ Observation Reveals Local Detachment Mechanisms and Suction Effects in Micropatterned Adhesives. *Adv. Funct. Mater.* **2019**, *29*, No. 1807713.

(9) Paretkar, D.; Kamperman, M.; Schneider, A. S.; Martina, D.; Creton, C.; Arzt, E. Bioinspired Pressure Actuated Adhesive System. *Mater. Sci. Eng., C* **2011**, *31*, 1152−1159.

(10) Tinnemann, V.; Arzt, E.; Hensel, R. Switchable Double-Sided Micropatterned Adhesives for Selective Fixation and Detachment. *J. Mech. Phys. Solids* **2019**, *123*, 20−27.

(11) Frensemeier, M.; Kaiser, J. S.; Frick, C. P.; Schneider, A. S.; Arzt, E.; Fertig, R. S.; Kroner, E. Temperature-Induced Switchable Adhesion Using Nickel-Titanium-Polydimethylsiloxane Hybrid Surfaces. *Adv. Funct. Mater.* **2015**, *25*, 3013−3021.

(12) Reddy, S.; Arzt, E.; Del Campo, A. Bioinspired Surfaces with Switchable Adhesion. *Adv. Mater.* **2007**, *19*, 3833−3837.

(13) Krahn, J.; Bovero, E.; Menon, C. Magnetic Field Switchable Dry Adhesives. *ACS Appl. Mater. Interfaces* **2015**, *7*, 2214−2222.

(14) Drotlef, D. M.; Blümler, P.; Del Campo, A. Magnetically Actuated Patterns for Bioinspired Reversible Adhesion (Dry and Wet). *Adv. Mater.* **2014**, *26*, 775−779.

(15) Nadermann, N.; Ning, J.; Jagota, A.; Hui, C.-Y. Active Switching of Adhesion in a Film-Terminated Fibrillar Structure. *Langmuir* **2010**, *26*, 15464−15471.

(16) Kizilkan, E.; Strueben, J.; Staubitz, A.; Gorb, S. N. Bioinspired Photocontrollable Microstructured Transport Device. *Sci. Rob.* **2017**, *2*, No. eaak9454.

(17) Shintake, J.; Rosset, S.; Schubert, B.; Floreano, D.; Shea, H. Versatile Soft Grippers with Intrinsic Electroadhesion Based on Multifunctional Polymer Actuators. *Adv. Mater.* **2016**, *28*, 231−238.

(18) Guo, J.; Bamber, T.; Chamberlain, M.; Justham, L.; Jackson, M. Optimization and Experimental Verification of Coplanar Interdigital Electroadhesives. *J. Phys. D: Appl. Phys.* **2016**, *49*, No. 415304.

(19) Persson, B. N. J.; Guo, J. Electroadhesion for Soft Adhesive Pads and Robotics: Theory and Numerical Results. *Soft Matter* **2019**, *15*, 8032−8039.

(20) Asano, K.; Hatakeyama, F.; Yatsuzuka, K. Fundamental Study of an Electrostatic Chuck for Silicon Wafer Handling. *IEEE Trans. Ind. Appl.* **2002**, *38*, 840−845.
(21) Monkman, G. Electroadhesive Microgrippers. *Ind. Rob.* **2003**, *30*, 326−330.
(22) Cao, C.; Sun, X.; Fang, Y.; Qin, Q.- H.; Yu, A.; Feng, X.-Q. Theoretical Model and Design of Electroadhesive Pad with Interdigitated Electrodes. *Mater. Des.* **2016**, *89*, 485−491.
(23) Prahlad, H.; Pelrine, R.; Stanford, S.; Marlow, J.; Kornbluh, R. In *Electroadhesive Robots - Wall Climbing Robots Enabled by a Novel, Robust, and Electrically Controllable Adhesion Technology*, International Conference on Robotics and Automation; IEEE: Pasadena, CA, 2008; pp 3028−3033.
(24) Shintake, J.; Cacucciolo, V.; Floreano, D.; Shea, H. Soft Robotic Grippers. *Adv. Mater.* **2018**, *30*, No. 1707035.
(25) Krahn, J.; Menon, C. Electro-Dry-Adhesion. *Langmuir* **2012**, *28*, 5438−5443.
(26) Ruffatto, D.; Parness, A.; Spenko, M. Improving Controllable Adhesion on Both Rough and Smooth Surfaces with a Hybrid Electrostatic/Gecko-like Adhesive. *J. R. Soc., Interface* **2014**, *11*, No. 20131089.
(27) Schargott, M.; Popov, V. L.; Gorb, S. Spring Model of Biological Attachment Pads. *J. Theor. Biol.* **2006**, *243*, 48−53.
(28) Zambakas, J. D.; Retalis, D. A.; Mavrakis, D. C. A Simultaneous Interpretation, by Wind Speed and Direction, of Ambient Air Polar Conductivities in Athens, Greece. *Arch. Meteorol., Geophys. Bioclimatol., Ser. A* **1985**, *33*, 381−388.
(29) Smith, L. G.; Schilling, G. F. The Variation of Electrical Conductivity of Air within Sealed Rooms. *J. Atmos. Terr. Phys.* **1954**, *4*, 314−321.
(30) Mark, J. *Polymer Data Handbook*, 2nd ed.; Mark, J. E., Ed.; Oxford University Press: New York, New York, USA, 2009.
(31) Morey, G. W. *The Property of Glass*; American Chemistry Society Monograph Series, Reinhold, Publ. Corp, 1954.
(32) Warburg, E.; Ihmori, T. Ueber das Gewicht und die Ursache der Wasserhaut bei Glas und anderen Körpern. *Ann. Phys. Chem.* **1886**, *263*, 481−507.
(33) Awakuni, Y.; Calderwood, J. H. Water Vapour Adsorption and Surface Conductivity in Solids. *J. Phys. D. Appl. Phys.* **1972**, *5*, 1038−1045.
(34) Skinner, B.; Loth, M. S.; Shklovksii, B. I. Ionic Conductivity on a Wetting Surface. *Phys. Rev. E* **2009**, *80*, No. 041925.
(35) Curtis, H. L. Insulating Properties of Solid Dielectrics. *Bull. Bur. Stand.* **1915**, *11*, 359.
(36) Woodson, H. H.; Melcher, J. R. *Electromechanical Dynamics*; Wiley, 1968.
(37) Arnoldus, H. F. Conservation of Charge at an Interface. *Opt. Commun.* **2006**, *265*, 52−59.
(38) Castellanos, A.; Gonzalez, A. Nonlinear Electrohydrodynamics of Free Surfaces. *IEEE Trans. Dielectr. Electr. Insul.* **1998**, *5*, 334−343.
(39) Carlon, H. R. *Electrical Properties of Atmospheric Moist Air: A Systematic,Experimental Study*; U.S. Army Technical Report No. CRDEC-TR-88059, 1988.
(40) Cobb, W. E.; Wells, H. J. The Electrical Conductivity of Oceanic Air and Its Correlation to Global Atmospheric Pollution. *J. Atmos. Sci.* **1970**, *27*, 814−819.
(41) Sampath, S.; Sasi Kumar, V.; Murali Das, S. Airborne Measurements of Atmospheric Electrical Conductivities. *Pure Appl. Geophys.* **1994**, *143*, 713−727.
(42) Van Hippel, A. *Tables of Dielectric Materials*; MIT Cambridge, Labortory for Insulation Research, 1944.
(43) Deyhimi, F.; Munoz, J.-L. Surface Resistivity of Different Silylated Glasses. *J. Appl. Electrochem.* **1984**, *14*, 803−806.
(44) Paiva, V. T. C.; Santos, L. P.; da Silva, D. S.; Burgo, T. A. L.; Galembeck, F. Conduction and Excess Charge in Silicate Glass/Air Interfaces. *Langmuir* **2019**, *35*, 7703−7712.
(45) Moulson, A. J.; Herbert, J. M. *Electroceramics: Materials, Properties, Applications*; John Wiley & Sons, 2003.
(46) Shackelford, J. F.; Han, Y.-H.; Kim, S.; Kwon, S.-H. *CRC Materials Science and Engineering Handbook*; CRC Press, 2016.
(47) Marcuse, D. Electrostatic Field of Coplanar Lines Computed with the Point Matching Method. *IEEE J. Quantum Electron.* **1989**, *25*, 939−947.
(48) Xu, L.; Wu, H.; Yao, G.; Chen, L.; Yang, X.; Chen, B.; Huang, X.; Zhong, W.; Chen, X.; Yin, Z.; Wang, Z. L.; et al. Giant Voltage Enhancement via Triboelectric Charge Supplement Channel for Self-Powered Electroadhesion. *ACS Nano* **2018**, *12*, 10262−10271.
(49) Guo, J.; Tailor, M.; Bamber, T.; Chamberlain, M.; Justham, L.; Jackson, M. Investigation of Relationship between Interfacial Electroadhesive Force and Surface Texture. *J. Phys. D. Appl. Phys.* **2016**, *49*, No. 035303.
(50) Krape, R. P. *Applications Study of Electroadhesive Devices*, NASA Contractor Report, CR-1211; National Aeronautics and Space Administration, 1968.
(51) Kroner, E.; Maboudian, R.; Arzt, E. Adhesion Characteristics of Pdms Surfaces during Repeated Pull-off Force Measurements. *Adv. Eng. Mater.* **2010**, *12*, 398−404.

https://dx.doi.org/10.1021/acsami.0c05077
ACS Appl. Mater. Interfaces 2020, 12, 27708−27716